www.acsanm.org Article

Development of Phosphorus-Doped Nanoscale Poly-Si Passivating Contacts via Inkjet Printing for Application in Silicon Solar Cells

Jiali Wang,* Sieu Pheng Phang, Christian Samundsett, Zhuofeng Li, Thien N. Truong, Jie Yang, Zhao Wang, Peiting Zheng, Xinyu Zhang, Hieu T. Nguyen, Daniel Macdonald, and Josua Stuckelberger

Cite This: ACS Appl. Nano Mater. 2023, 6, 140−147

Read Online

ACCESS | Metrics & More | Article Recommendations

ABSTRACT: Herein, high-quality localized phosphorus-doped polycrystalline silicon (poly-Si) passivating contacts containing nanoscale poly-Si film (∼100 nm) on an ultrathin SiO_x layer (∼1.5 nm) were fabricated via an inkjet printing technique. A detailed study of the impacts of inkjet printer settings, dopant concentration, and annealing temperature on the poly-Si passivating contact performance (represented by implied open-circuit voltage iV_{oc} and contact resistivity ρ_c) was carried out. By applying optimized process conditions on symmetrical industrially processed intrinsic poly-Si/SiO_x/n-type crystalline Si (c-Si) substrates, good surface passivation was achieved with an iV_{oc} of 699 mV, together with a low ρ_c of 6.4 mΩ·cm^2, after annealing at 975 °C. After a hydrogenation treatment via the deposition of aluminum oxide (AlO_x)/silicon nitride (SiN_y) stack and subsequent forming gas annealing (FGA), the optimum annealing temperature shifted to 950 °C and the iV_{oc} was further improved to an excellent value of 729 mV. Optical images reveal that a line width of 75 μm can be realized on a mechanically polished silicon wafer. Moreover, high-resolution micro-photoluminescence (μ-PL) maps clearly demonstrate the localization of the doped regions on the symmetrical substrate after annealing. These results show that inkjet printing is a promising technique for the fabrication of localized poly-Si/SiO_x passivating contacts in high-efficiency solar cells with high flexibility and simplicity.

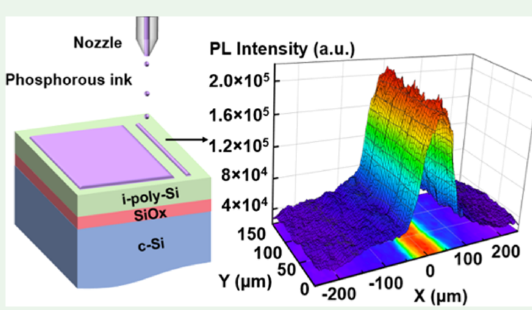

KEYWORDS: *inkjet-printed doping, liquid doping, ex-situ doping, passivating contact, silicon solar cell*

Downloaded via AUSTRALIAN NATL UNIV on January 31, 2023 at 23:38:50 (UTC).
See https://pubs.acs.org/sharingguidelines for options on how to legitimately share published articles.

1. INTRODUCTION

Solar photovoltaic is one of the fastest-growing renewable energy technologies, exceeding a generation of 1000 TWh in 2021.[1] Over the years, improving the conversion efficiency and reducing the cost of manufacturing have been key research objectives in the photovoltaic community. Nowadays, silicon solar cells incorporating polycrystalline silicon (poly-Si) passivating contacts, combining a nanoscale ultrathin SiO_x layer and a doped poly-Si film in a stacked structure, have demonstrated significant improvements in conversion efficiencies and are expected to grow rapidly in the market share.[2] This structure has proven to remarkably reduce carrier recombination at the metal−silicon interface while retaining a low contact resistance.[3,4] Compared to conventional dopant-diffused contacts, the recombination at the metal−silicon junction is screened by an additional high band gap layer between the metal contact and the c-Si wafer. This nanoscale interfacial layer presents a barrier to the charge carriers and reduces interface traps.[3] The structure is referred to by several names, such as tunnel oxide passivated contacts (TOPCon),[5,6] polycrystalline silicon on oxide (POLO),[7,8] and poly-Si passivating contacts.[9−11] At the laboratory scale, by applying this approach, efficiencies above 26% have been achieved with both-sides contacted solar cells[12] and with an interdigitated back contact cell structure.[13] Poly-Si passivating contacts have also already been successfully implemented in industry, reaching an efficiency of 25.4% on full-sized wafers.[14] These promising achievements indicate the great potential of this structure and the importance of further developing this concept.[12]

The poly-Si layer can be doped via various technologies and different dopant sources. They are often categorized as *in-situ* and *ex-situ* doping. *In-situ* methods introduce the dopants simultaneously with the deposition of the poly-Si layer by plasma-enhanced chemical vapor deposition (PECVD),[15−17] low-pressure chemical vapor deposition (LPCVD), or physical vapor deposition (PVD).[18] *Ex-situ* doping methods utilize gas dopants (BBr_3 or $POCl_3$ gases),[19,20] ion implantation,[21−23] or liquid dopants.[24−26] One of the drawbacks of gas doping

Received: September 19, 2022
Accepted: November 22, 2022
Published: December 7, 2022

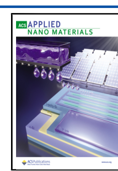

© 2022 American Chemical Society

https://doi.org/10.1021/acsanm.2c04148
ACS Appl. Nano Mater. 2023, 6, 140−147

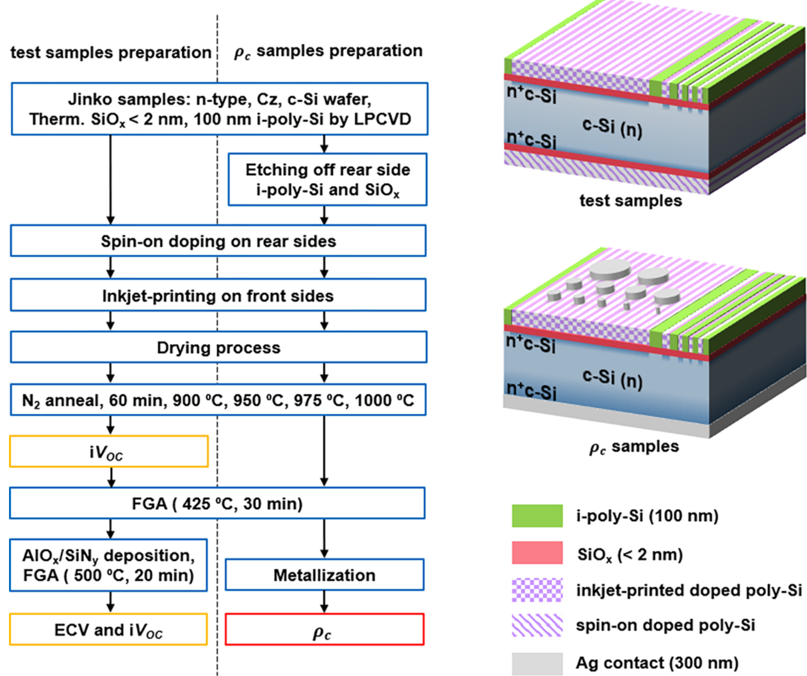

Figure 1. Process flows and schematic structures for test samples and samples for contact resistivity measurements (ρ_c samples).

methods is the challenge of achieving single-sided doping, as the other side must be masked. One potential solution is the use of liquid dopants in a spin-coater. In 2017, Fogel applied the spin-coating technique to dope poly-Si layers using P, B, and Ga dopants, achieving an iV_{oc} of 727 mV for n-type, P-doped passivating contacts.[27] Recently, Yang et al. have reached a power conversion efficiency of 18.5% by spin-coating the poly-Si layer with commercial P and B-doped solutions on each side of the substrate.[28] Ding et al. have also proven the effectiveness of spin-on doping on industrially fabricated samples by reaching iV_{oc} values of 730 and 720 mV for P-doped and B-doped poly-Si passivating contacts, respectively.[25,29]

An alternative way to implement liquid doping is to print the liquid dopant via an inkjet printer. In 2021, Kiaee et al. successfully fabricated n-type poly-Si passivating contacts using a PiXDRO LP50 inkjet printer with phosphorus ink, reporting an impressive iV_{oc} of 733 mV.[30] In addition to achieving excellent passivation, the most unique advantage of this approach is the capability for forming localized poly-Si passivating contacts without costly masking processes. Recently, by printing phosphorus dopant lines with a width of around 300 μm underneath the screen-printed metal fingers, Kiaee et al. applied inkjet-printing technology to selectively dope n-type TOPCon layers on industrial solar cells for the first time, with a promising conversion efficiency of 22.0%.[31] Their achievements demonstrated that inkjet-printed doping can be an effective method to fabricate poly-Si passivating contacts.

Nevertheless, more work is required to optimize the high-temperature annealing processes, narrow the printed line width, and eliminate the outgassing of dopants from the printed region,[31] in order to achieve higher-efficiency silicon solar cells. In this work, we employed a FUJIFILM Material Printer DMP-2850 to fabricate n-type poly-Si passivating contacts. We first optimize the inkjet printing parameters to ensure a sufficient supply of dopants to the nanoscale poly-Si layer, and then investigate the effects of annealing temperature on the performance of printed poly-Si contacts. Moreover, we explored the ability of forming narrow localized contacts by printing thin dopant lines with a width of 75 μm. Their performance was observed and characterized by optical microscopy, photoluminescence (PL) imaging, and high-resolution micro-photoluminescence (μ-PL) mapping techniques. The mapping results reveal the band-to-band PL emission variation along the annealed dopant line, providing a pathway to assess the outgassing effect while optimizing the fabrication processes.

2. EXPERIMENTAL DETAILS

The experiments were conducted on industrially prepared symmetrical intrinsic poly-Si (i-poly-Si) samples, with the process flow shown in Figure 1. The wafers were (100)-oriented n-type Czochralski-grown (Cz) silicon wafers with a resistivity of 1.5 Ω·cm and a thickness of 150 μm. After saw damage etching and standard Radio Corporation of America (RCA) cleaning, an ultrathin SiO_x layer (<2 nm) was grown by thermal oxidation in a tube furnace at 600 °C for 5 min. Subsequently, 100 nm thick i-poly-Si layers were deposited on the SiO_x layers by LPCVD. The samples were processed up to this stage by Jinko Solar using industrial fabrication tools. The samples were then laser cut into 5 cm × 5 cm pieces for ease of processing in subsequent steps.

After RCA cleaning, the spin-coating control samples were coated with phosphorus-containing spin-on-glass (SOG) solution (P-250, [P] 5×10^{21} cm^{-3}, Desert Silicon) on both sides using a spin coater (Laurell WS-650-23NPPB). For the inkjet printing test samples, one side was coated by the spin-coater, whereas the other side was printed with SOG ink using the inkjet printer. The inkjet-printed pattern is a 4 cm × 3 cm dot array with drop spacing of either 10, 25, or 50 μm. We initially used the commercially available phosphorus SOG solution, but it resulted in poor printing performance. Considering that the fluid properties are critical for printability, we modified the SOG solution using glycol to increase the viscosity and decrease the evaporation rate. The ink was created by mixing the SOG solution with glycol, with a volume ratio of 0.5, 0.75, and 0.9 of SOG in the mixed solution, hereafter referred to as 0.5 ratio solution, 0.75 ratio

https://doi.org/10.1021/acsanm.2c04148
ACS Appl. Nano Mater. 2023, 6, 140−147

solution, and 0.9 ratio solution, respectively. Thereafter, the drying processes consisted of soft baking at 90 °C for 10 min in an oven and hard baking at 200 °C for 6 min on a hotplate. Afterwards, the samples were annealed in N_2 atmosphere for 60 min at temperatures ranging from 900 to 1000 °C.

Next, the samples were hydrogenated using forming gas annealing (FGA, 5% H_2, 95% Ar) at 425 °C for 30 min. Phosphorus−silica glasses were then removed using 5% hydrofluoric acid (HF) solution. Subsequently, wafers were subjected to further hydrogenation by depositing layers of aluminum oxide (AlO_x) and silicon nitride (SiN_y) followed by an additional FGA at 500 °C for 20 min. Atomic layer deposition (ALD) and PECVD were used to deposit the AlO_x and SiN_y films, respectively. Finally, the stacks were removed by dipping in buffered HF (BHF; ammonium fluoride (NH_4F) and HF) solution for 7 min. The schematic structure of the test samples is shown in Figure 1.

The iV_{oc} was measured by the photoconductance decay (PCD) technique with a Sinton WCT-120 lifetime tester, both before the first FGA (425 °C) and in the final state after dipping in the BHF.[32] The active dopant profiles were measured after the BHF dip by the electrochemical capacitance−voltage (ECV) method using a WEP Wafer Profiler CVP21. In addition, contact resistivity values were obtained using the Cox and Strack method with a Keithley Sourcemeter 2400.[33] A sample set specially for contact resistivity measurements was prepared in addition to the test samples. For these samples, the i-poly-Si and SiO_x layers on the rear side were etched off before doping. After the removal of the i-poly-Si and SiO_x layers, these samples experienced the same treatments as the test samples up to the 425 °C FGA, including the spin coating of SOG on the rear surface, which leads to a heavily doped surface region within the wafer ensuring good contact between the metal and the wafer on the rear side. Subsequently, 300 nm thick circular silver pads with different diameters were formed on the front side of the sample using thermal evaporation with a shadow mask, while the full area of the rear side was covered by 300 nm of silver. The diameters of the eleven circular pads were 0.5, 1, 1.5, 2, 2.5, 3, 3.5, 4, 5, 6, and 8 mm.

After examining the passivation quality of the poly-Si contacts fabricated by the inkjet-printed doping technique, its performance for localized printing was investigated using optical microscopy, PL imaging, and high-resolution μ-PL mapping. We first studied the size of single droplets and analyzed a 75 μm wide printed line on a mechanically polished 100-oriented bare Si wafer using an optical microscope directly after printing. Polished substrates were used for clearer visualization of the printed lines. In addition, the 75 μm wide line was printed on a sample with the same structure as the test samples mentioned in Section 2 for PL imaging and μ-PL mapping. The sample was subjected to the drying processes and 975 °C annealing before being measured. In this work, we imaged the Si band-to-band PL intensity using a BT imaging LIS-R1 system with a spatial resolution of 22 μm per pixel. We then mapped the Si band-to-band PL emission at room temperature with a Horiba LabRAM system. It is equipped with a confocal microscope and a liquid-nitrogen-cooled InGaAs detector (detection range between 900 and 1600 nm) and a 10× objective lens. The excitation source was a continuous-wave 532 nm diode-pumped solid-state (DPSS) laser. The laser light was focused onto the sample surface with a diameter of around 2.5 μm and the on-sample excitation power was about 2 mW. The mapping step in the horizontal direction and the vertical direction is 2 and 5 μm, respectively. The much higher illumination intensity in the μ-PL mapping compared to the PL imaging reduces lateral carrier diffusion effects and allows a sharper observation of the heavily doped regions.

3. RESULTS AND DISCUSSION

3.1. Printing Process Development. The printing process development aims to identify the optimal inkjet printing parameters. To achieve the desired passivation quality, sufficient dopants should be introduced. The built-in drop watcher facilitates the optimization of printing parameters by enabling real-time observation of drop formation. In this way, we determine the optimal jetting frequency and jetting voltage for solutions of different mixing ratios to produce round droplets without excess ink or blocked nozzles. Figure 2a shows an optical microscope image of individual drops printed on a mechanically polished 100-orientated bare Si wafer using a 10 pL cartridge and 0.75 ratio solution. According to the image, the printed drops are of circular shape, with a diameter of around 25 μm. The drop spacing (resolution) describes the center-to-center distance from one drop to the next, which enables full coverage when it reaches the drop diameter. Theoretically, when using a drop spacing of 25 μm, the drops would contact adjacent drops, leading to the formation of a 75 μm thick drop array by having three drops in the vertical direction, as illustrated in Figure 2b. In practice, the printed drops coalesce on the sample surface, filling the gaps between drops and resulting in a 74.2 μm line, as shown in Figure 2c. In the same manner, by setting the drop spacing as the corresponding drop diameter for each jetting condition, the sample surface is fully covered by the solution. This strategy may not be suitable for textured surfaces with pyramids of typical size,[34−36] as the surface roughness would greatly influence the interactions of the surface and droplets leading to different spreading and coalescing.[37−39] However, we expect a continuous film formation to be achievable through adjustments in inkjet printing parameters including jetting voltage (directly correlated to the drop size), frequency, and drop spacing.

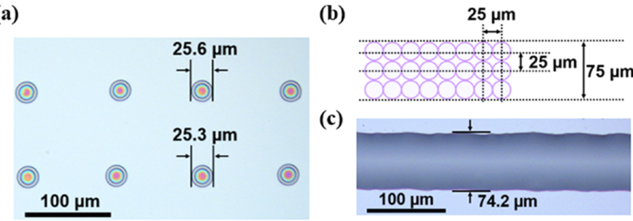

Figure 2. Optical microscope image of (a) drops (c) line printed by a 10 pL cartridge and 0.75 ratio solution on a mechanically polished 100-orientated bare Si wafer. (b) Schematic of a drop array formed by reducing the drop spacing to 25 μm.

From doping profiles reported in the literature[25,29,30] and on our SOG-control sample, we aim for a doping concentration within the poly-Si in the range of $1-5 \times 10^{20}$ cm^{-3}, with a rapid drop-off within the c-Si wafer. The high concentration within the poly-Si layer enables the desired band-bending, while a strong in-diffusion into the c-Si wafer may damage the SiO_x interlayer and can lead to enhanced Auger recombination.[4,23,40] The printed and SOG-control samples studied in the printing process development follow the fabrication steps described in Section 2 and all were annealed at 950 °C. The active dopant profiles for test samples and the SOG-control sample were measured from the printed front surfaces after the first FGA and are shown in Figure 3.

First prints were performed using a 1 pL cartridge with 0.5 ratio solution and 10 μm drop spacing but only achieved a doping level in the poly-Si layer below 10^{19} cm^{-3}, which is more than an order of magnitude lower than the SOG-control sample. Consequently, the passivation quality is poor with a low iV_{oc} of 544 mV. Two additional prints with the same settings (three printed layers in total) increased the doping level slightly to above 10^{19} cm^{-3}. By using a higher solution

https://doi.org/10.1021/acsanm.2c04148
ACS Appl. Nano Mater. 2023, 6, 140−147

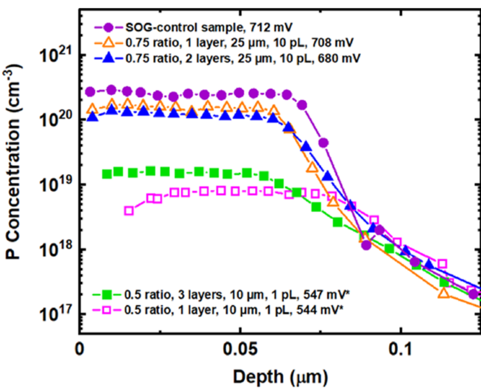

Figure 3. Active dopant concentration measured after the first FGA for samples printed with various inkjet parameters annealed at 950 °C. Round symbols show the SOG-control sample, square symbols represent samples printed with the 0.5 ratio solution, while triangular symbols illustrate the 0.75 ratio solution. Open symbols and solid symbols indicate that the sample is single-printed or multiple-printed, respectively. Legends also include the drop spacing (10, 25, and 50 μm), cartridge dimension (1 and 10 pL), and iV_{oc} values after the first FGA. * Samples inkjet-printed symmetrically without spin-on coating. This does not affect the ECV results but influences the measured iV_{oc}.

ratio of 0.75 in combination with a 10 pL cartridge, the doping level and iV_{oc} were improved and approached a similar value to the SOG-control sample. However, multiple printings using the 0.75 ratio solution did not result in a further increase in the doping concentration. On the other hand, multiple prints increase fabrication time and cost and reduce the printing resolution, so single printing with a higher solution ratio is preferred. Although the improvement in doping concentration from a higher solution ratio is clear, it should be noted that the 100% SOG solution is incompatible with our printing setup because of its low viscosity and high evaporation rate. Therefore, the maximum volume ratio was limited to 0.9 in the next experiment on the effect of annealing conditions. Inkjet parameters were set at 25 μm drop spacing using the 10 pL cartridge in the following experiment.

3.2. Influence of Annealing Temperature. Figure 4a presents the impacts of the annealing temperature and solution concentration on the iV_{oc} values of poly-Si passivating contacts measured after annealing and after hydrogenation via AlO_x/SiN_y stacks. Although obvious improvements in the doping concentration and iV_{oc} were observed when increasing the solution ratio from 0.5 to 0.75 in the previous section, there is no significant difference in the iV_{oc} values of samples printed with the 0.75 ratio solution and the 0.9 ratio solution. This might imply that the effect of the solution ratio or the doping concentration has saturated at 0.75 ratio, which is supported by no further increase in the doping concentration for the 0.9 ratio as measured by ECV. The excess P atoms remain in the glass layers and are not driven-in during annealing.

The annealing temperature has a significant influence on the passivation quality. For samples measured after annealing in the N_2 atmosphere, the iV_{oc} values increase steadily from 900 up to 975 °C and then decrease strongly for annealing at 1000 °C. The samples printed with 0.75 ratio solution and 0.9 ratio solution showed high iV_{oc} values of 699 and 692 mV, respectively, at 975 °C. The subsequent hydrogenation boosted the iV_{oc} values across the range of annealing temperatures used, especially for samples annealed at 950 °C. After hydrogenation, the optimum annealing temperature shifted to 950 °C, with excellent iV_{oc} values of 729 mV achieved on samples printed with both the 0.75 ratio solution and the 0.9 ratio solution. However, hydrogenation has only a minor impact on annealing temperatures at 1000 °C. The iV_{oc} trend observed from this experiment bears a resemblance to the results obtained by Ding et al., who adopted the spin-on doping method to fabricate phosphorus-doped poly-Si passivating contacts. The iV_{oc} values of their spin-on doped samples increased with the annealing temperature from 900 to 975 °C. Then, similarly, a remarkable drop in iV_{oc} also occurred when the annealing temperature approached 1000 °C.[25]

By examining the active doping concentration profiles, as shown for the 0.75 ratio printed samples in Figure 4b, the iV_{oc} variation with annealing temperatures can be explained. Higher temperatures enable more P atoms to diffuse into the c-Si substrate, suppressing the minority carrier density near the SiO_x/c-Si interface and reducing the interface carrier recombination. However, when the annealing temperature approaches 975 °C, the SiO_x layer likely disrupts locally and the increased in-diffusion of P leads to slightly increased Auger recombination,[41] resulting in a decrease in passivation quality. Increasing the annealing temperatures further to 1000 °C disrupted the nanoscale ultrathin SiO_x layer significantly, as evidenced by the strong in-diffusion into the c-Si bulk, leading

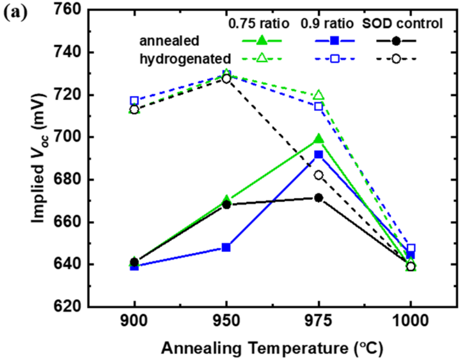

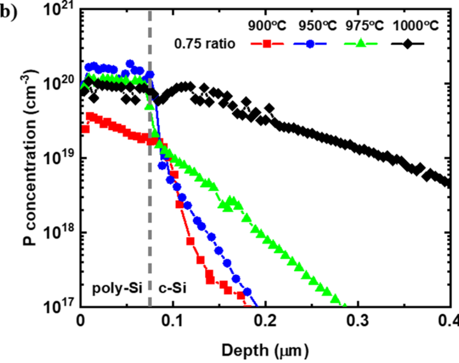

Figure 4. (a) iV_{oc} values for phosphorus-doped samples printed by 0.75 (green lines) and 0.9 (blue lines) ratio solutions together with SOG-control samples (black lines) at different annealing temperatures after annealing (solid lines) and after hydrogenation via an AlO_x/SiN_y stack (dashed lines). (b) Active dopant concentrations for samples printed with 0.75 ratio solution annealed at different temperatures. Dashed line indicates the position of the SiO_x interlayer.

to a strong decrease in iV_{oc}. The severe degradation at 1000 °C was difficult to passivate by hydrogenation. Furthermore, the effectiveness of hydrogenation via an AlO_x/SiN_y stack generally decreases with annealing temperature (see Figure 4a). The higher the annealing temperature, the more dominant the field-effect passivation (i.e., the less dominant the chemical passivation) because there are more dopants in the near-surface region of the Si substrate (Figure 4b). Therefore, hydrogen passivation of defects has less impact on recombination. Besides, the doping level in the poly-Si layer increases with the highest concentration at 950 °C before it decreases with higher temperatures. This might imply that the inkjet-printed glass was depleted at higher temperatures.

Figure 5 below presents the contact resistivities of samples, which excludes the samples annealed at 900 °C, as the $I-V$ curves obtained from the Cox and Strack measurements were nonlinear, hinting at a poor ohmic contact. According to the results, no clear trend is observed for the contact resistivities as a function of the annealing temperature above 950 °C; nevertheless, all the contact resistivities of the fabricated samples remain at a low level below 7 mΩ·cm^2.

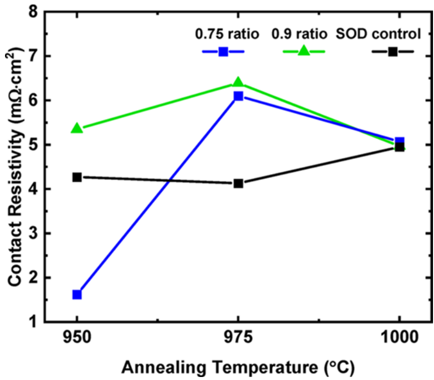

Figure 5. Contact resistivity values of samples examined using the Cox and Strack method. It is to be noted that the contact resistivity was measured after the first FGA.

This is in a similar range as reported for high-performing PERC cells[42,43] or poly-Si contacts fabricated by conventional doping methods.[44,45] Therefore, it is well suited to be implemented under local metallization using typical front grid designs, along with suitable technologies for localizing poly-Si under the contacts. Inkjet printing will also be suitable for rear surface poly-Si, enabling selective doping of poly-Si. The lower doping in noncontacted poly-Si regions would reduce free carrier absorption and parasitic absorption. IBC structures would also be a promising approach for the implementation. The achieved contact resistivity would still cause a drop in the fill factor (FF) with a reduced area fraction of metallization.[41] Therefore, optimization in the area fraction for contacts is necessary to maximize the conversion efficiency.[46]

3.3. Localized Printing Performance. Figure 6 shows the photoluminescence analysis of a printed line on a symmetrical industrial poly-Si sample presented in Section 2 after 975 °C annealing. In Figure 6a, the PL image is captured by a BT imaging LIS-R1 system using a magnification lens, showing a printed line, three droplets wide, as presented in Section 3.1 with a targeted line width of 75 μm. The line width is difficult to define because of lateral carrier diffusion effects, which are significant under these relatively low-intensity illumination conditions. To reduce these carrier diffusion effects, Figure 6b,c show the integrated band-to-band PL intensity map measured by a Horiba Lab RAM μ-PL system, which uses a much higher illumination intensity, and hence the injection level. The PL intensities were integrated over wavelengths from 1050 to 1250 nm. The higher emitted PL intensity in the doped regions is due to the locally improved surface passivation, leading to a higher band-to-band PL intensity from the wafer below. The PL intensity profile averaged from Y = 90 to 100 is plotted in Figure 6c, the PL intensity remains above 90% of the maximum value over a width of 45 μm, and then steeply drops to 20% of the maximum value over a further distance of approximately 30 μm on each side. Below the 20% level, the PL intensity experiences a shallow change on each side of the peak, gradually reducing to the baseline intensity. This may be due to the lateral movement of phosphorus dopants. Nevertheless, it is observed that the full width at half maximum of the averaged PL intensity profile is around 80 μm, which is close to the target line width (75 μm).

The achieved width of the heavily doped region is promising in comparison to those used in the IBC solar cells with POLO passivating contacts for both polarities, as demonstrated by Hollemann et al., where the n-type and p-type POLO contact widths were 270 and 120 μm, respectively.[47] This illustrates the printer's capability of localized printing and therefore

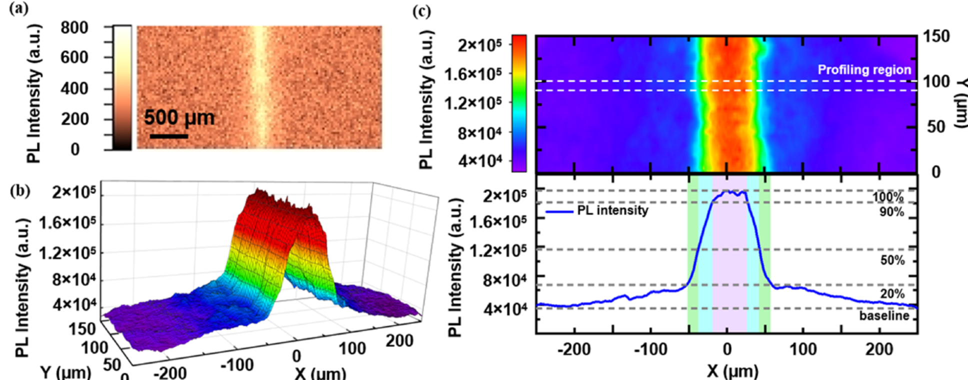

Figure 6. (a) PL image of a line printed by a 10 pL cartridge and 0.75 ratio solution on the poly-Si substrate, with a target line width of 75 μm. The sample was excited at 10 suns for 25 s. (b) Higher-resolution μ-PL intensity map of the printed line. (c) μ-PL intensity map of the printed line in the 2D version. Averaged intensity profile from Y = 90 to 100 μm is presented below the map.

https://doi.org/10.1021/acsanm.2c04148
ACS Appl. Nano Mater. 2023, 6, 140−147

passivation with the required precision for high-efficiency IBC silicon solar cells. By adjusting the inkjet parameters, various line widths can be realized, which increases the flexibility in solar cell design.

4. CONCLUSIONS

We have applied inkjet printing technology to enable localized doping of poly-Si passivating contacts for c-Si solar cells, with results comparable to those of other state-of-the-art doping methods. After adjusting the inkjet-printing parameters to maximize the doping concentration within the 100 nm poly-Si layer, we studied the impacts of annealing temperature and achieved excellent passivation quality with an iV_{oc} of 729 mV in combination with a low contact resistivity below 7 mΩ·cm^2 for an annealing temperature of 950 °C using a SOG liquid source with 0.75 and 0.9 volume ratios mixed with glycol. The breakdown of the ultrathin SiO_x layer was observed at annealing temperatures of 975 and 1000 °C. Meanwhile, the printer's ability to create localized printing has been investigated using optical microscopy and μ-PL mapping. In this way, we demonstrate the potential application of the inkjet-printed doping technique for simple, fast, and maskless fabrication of high-efficiency silicon solar cells with localized poly-Si contacts, such as IBC cells.

AUTHOR INFORMATION

Corresponding Author

Jiali Wang − *School of Engineering, The Australian National University, Canberra, ACT 2600, Australia;* orcid.org/0000-0002-5050-3082; Email: Jiali.Wang1@anu.edu.au

Authors

Sieu Pheng Phang − *School of Engineering, The Australian National University, Canberra, ACT 2600, Australia*

Christian Samundsett − *School of Engineering, The Australian National University, Canberra, ACT 2600, Australia*

Zhuofeng Li − *School of Engineering, The Australian National University, Canberra, ACT 2600, Australia*

Thien N. Truong − *School of Engineering, The Australian National University, Canberra, ACT 2600, Australia;* orcid.org/0000-0002-4082-7999

Jie Yang − *Zhejiang Jinko Solar Co., Ltd, Jiaxing, Zhejiang 314416, China*

Zhao Wang − *Zhejiang Jinko Solar Co., Ltd, Jiaxing, Zhejiang 314416, China*

Peiting Zheng − *Zhejiang Jinko Solar Co., Ltd, Jiaxing, Zhejiang 314416, China*

Xinyu Zhang − *Jinko Solar Co., Ltd, Shangrao, Jiangxi 334100, China*

Hieu T. Nguyen − *School of Engineering, The Australian National University, Canberra, ACT 2600, Australia;* orcid.org/0000-0003-1667-1135

Daniel Macdonald − *School of Engineering, The Australian National University, Canberra, ACT 2600, Australia*

Josua Stuckelberger − *School of Engineering, The Australian National University, Canberra, ACT 2600, Australia*

Complete contact information is available at: https://pubs.acs.org/10.1021/acsanm.2c04148

Author Contributions

All authors have given approval to the final version of the manuscript.

Notes

The authors declare no competing financial interest.

ACKNOWLEDGMENTS

We acknowledge the Australian National Fabrication Facility (ANFF) for the access to ALD and PECVD tools. J.S. and H.T.N. acknowledge fellowship support from the Australian Centre for Advanced Photovoltaics (ACAP).

ABBREVIATIONS

ALD, atomic layer deposition
BHF, buffered hydrofluoric acid
Cz, Czochralski-grown
DPSS, diode-pumped solid state
ECV, electrochemical capacitance−voltage
FF, fill factor
FGA, forming gas annealing
LPCVD, low-pressure chemical vapor deposition
PCD, photoconductance decay
PECVD, plasma-enhanced chemical vapor deposition
PL, photoluminescence
POLO, polycrystalline silicon on oxide
PVD, physical vapor deposition
RCA, radio corporative of America
SOG, spin-on glass
TOPCon, tunnel oxide passivated contact

REFERENCES

(1) International Energy Agency (IEA), *Solar PV*, September 2022. https://www.iea.org/reports/solar-pv (accessed November 2022).

(2) *International Technology Roadmap for Photovoltaic (ITRPV) 2021 Results*, 13th edition, March 2022. https://itrpv.vdma.org/ (accessed November 2022).

(3) Glunz, S. W.; Feldmann, F. SiO_2 surface passivation layers − a key technology for silicon solar cells. *Sol. Energy Mater. Sol. Cells* **2018**, *185*, 260−269.

(4) Richter, A.; Benick, J.; Müller, R.; Feldmann, F.; Reichel, C.; Hermle, M.; Glunz, S. W. Tunnel oxide passivating electron contacts as full-area rear emitter of high-efficiency p-type silicon solar cells. *Progr. Photovolt.: Res. Appl.* **2018**, *26*, 579−586.

(5) Feldmann, F.; Bivour, M.; Reichel, C.; Steinkemper, H.; Hermle, M.; Glunz, S. W. Tunnel oxide passivated contacts as an alternative to partial rear contacts. *Sol. Energy Mater. Sol. Cells* **2014**, *131*, 46−50.

(6) Zhang, Z.; Zeng, Y.; Jiang, C.-S.; Huang, Y.; Liao, M.; Tong, H.; Al-Jassim, M.; Gao, P.; Shou, C.; Zhou, X.; Yan, B.; Ye, J. Carrier transport through the ultrathin silicon-oxide layer in tunnel oxide passivated contact (TOPCon) c-Si solar cells. *Sol. Energy Mater. Sol. Cells* **2018**, *187*, 113−122.

(7) Haase, F.; Kiefer, F.; Schäfer, S.; Kruse, C.; Krügener, J.; Brendel, R.; Peibst, R. Interdigitated back contact solar cells with polycrystalline silicon on oxide passivating contacts for both polarities. *Jpn. J. Appl. Phys.* **2017**, *56*, No. 08MB15.

(8) Wehmeier, N.; Kiefer, F.; Brendeühl, T.; Mettner, L.; Wolter, S. J.; Haase, F.; Peibst, R.; Holthausen, M.; Mispelkamp, D.; Mader, C.; Daeschlein, C.; Wunnicke, O.; Kajari-Schröder, S. Inkjet-Printed In Situ Structured and Doped Polysilicon on Oxide Junctions. *IEEE J. Photovoltaics* **2021**, *11*, 1149−1157.

(9) Kang, D.; Sio, H. C.; Yan, D.; Stuckelberger, J.; Zhang, X.; Macdonald, D. Firing stability of phosphorus-doped polysilicon passivating contacts: Factors affecting the degradation behavior. *Sol. Energy Mater. Sol. Cells* **2022**, *234*, No. 111407.

(10) Liu, A.; Yan, D.; Phang, S. P.; Cuevas, A.; Macdonald, D. Effective impurity gettering by phosphorus- and boron-diffused polysilicon passivating contacts for silicon solar cells. *Sol. Energy Mater. Sol. Cells* **2018**, *179*, 136−141.

(11) Wu, H.; Stuckelberger, J.; Kang, D.; Chen, W.; Wang, W.; Samundsett, C.; Nguyen, H. T.; Macdonald, D. Micro-photoluminescence studies of shallow boron diffusions below polysilicon passivating contacts. *Sol. Energy Mater. Sol. Cells* **2021**, *227*, No. 111108.
(12) Richter, A.; Müller, R.; Benick, J.; Feldmann, F.; Steinhauser, B.; Reichel, C.; Fell, A.; Bivour, M.; Hermle, M.; Glunz, S. W. Design rules for high-efficiency both-sides-contacted silicon solar cells with balanced charge carrier transport and recombination losses. *Nat. Energy* **2021**, *6*, 429−438.
(13) Haase, F.; Hollemann, C.; Schäfer, S.; Merkle, A.; Rienäcker, M.; Krügener, J.; Brendel, R.; Peibst, R. Laser contact openings for local poly-Si-metal contacts enabling 26.1%-efficient POLO-IBC solar cells. *Sol. Energy Mater. Sol. Cells* **2018**, *186*, 184−193.
(14) JinkoSolar's High-efficiency N-Type Monocrystalline Silicon Solar Cell Sets New World Record with Highest Conversion Efficiency of 25.4% https://ir.jinkosolar.com/news-releases/news-release-details/jinkosolars-high-efficiency-n-type-monocrystalline-silicon-solar.
(15) Stuckelberger, J.; Nogay, G.; Wyss, P.; Jeangros, Q.; Allebé, C.; Debrot, F.; Niquille, X.; Ledinsky, M.; Fejfar, A.; Despeisse, M.; Haug, F.-J.; Löper, P.; Ballif, C. Passivating electron contact based on highly crystalline nanostructured silicon oxide layers for silicon solar cells. *Sol. Energy Mater. Sol. Cells* **2016**, *158*, 2−10.
(16) Nemeth, B.; Young, D. L.; Page, M. R.; LaSalvia, V.; Johnston, S.; Reedy, R.; Stradins, P. Polycrystalline silicon passivated tunneling contacts for high efficiency silicon solar cells. *J. Mater. Res.* **2016**, *31*, 671−681.
(17) Gao, T.; Yang, Q.; Guo, X.; Huang, Y.; Zhang, Z.; Wang, Z.; Liao, M.; Shou, C.; Zeng, Y.; Yan, B.; Hou, G.; Zhang, X.; Zhao, Y.; Ye, J. An industrially viable TOPCon structure with both ultra-thin SiO_x and n+−poly-Si processed by PECVD for p-type c-Si solar cells. *Sol. Energy Mater. Sol. Cells* **2019**, *200*, No. 109926.
(18) Yan, D.; Cuevas, A.; Phang, S. P.; Wan, Y.; Macdonald, D. 23% efficient p-type crystalline silicon solar cells with hole-selective passivating contacts based on physical vapor deposition of doped silicon films. *Appl. Phys. Lett.* **2018**, *113*, No. 061603.
(19) Truong, T. N.; Yan, D.; Chen, W.; Wang, W.; Guthrey, H.; Al-Jassim, M.; Cuevas, A.; Macdonald, D.; Nguyen, H. T. Deposition pressure dependent structural and optoelectronic properties of ex-situ boron-doped poly-Si/SiO_x passivating contacts based on sputtered silicon. *Sol. Energy Mater. Sol. Cells* **2020**, *215*, No. 110602.
(20) Park, H.; Park, H.; Park, S. J.; Bae, S.; Kim, H.; Yang, J. W.; Hyun, J. Y.; Lee, C. H.; Shin, S. H.; Kang, Y.; Lee, H.-S.; Kim, D. Passivation quality control in poly-Si/SiO_x/c-Si passivated contact solar cells with 734 mV implied open circuit voltage. *Sol. Energy Mater. Sol. Cells* **2019**, *189*, 21−26.
(21) Tetzlaff, D.; Krügener, J.; Larionova, Y.; Reiter, S.; Turcu, M.; Haase, F.; Brendel, R.; Peibst, R.; Höhne, U.; Kähler, J. D.; Wietler, T. F. A simple method for pinhole detection in carrier selective POLO-junctions for high efficiency silicon solar cells. *Sol. Energy Mater. Sol. Cells* **2017**, *173*, 106−110.
(22) Reichel, C.; Feldmann, F.; Müller, R.; Reedy, R. C.; Lee, B. G.; Young, D. L.; Stradins, P.; Hermle, M.; Glunz, S. W. Tunnel oxide passivated contacts formed by ion implantation for applications in silicon solar cells. *J. Appl. Phys.* **2015**, *118*, 205701.
(23) Yang, G.; Ingenito, A.; van Hameren, N.; Isabella, O.; Zeman, M. Design and application of ion-implanted polySi passivating contacts for interdigitated back contact c-Si solar cells. *Appl. Phys. Lett.* **2016**, *108*, No. 033903.
(24) Scardera, G.; Inns, D.; Wang, G.; Dugan, S.; Dee, J.; Dang, T.; Bendimerad, K.; Lemmi, F.; Antoniadis, H. All-screen-printed Dopant Paste Interdigitated Back Contact Solar Cell. *Energy Procedia* **2015**, *77*, 271−278.
(25) Ding, Z.; Yan, D.; Stuckelberger, J.; Phang, S. P.; Chen, W.; Samundsett, C.; Yang, J.; Wang, Z.; Zheng, P.; Zhang, X.; Wan, Y.; Macdonald, D. Phosphorus-doped polycrystalline silicon passivating contacts via spin-on doping. *Sol. Energy Mater. Sol. Cells* **2021**, *221*, No. 110902.
(26) Zhu, Z. -T.; Menard, E.; Hurley, K.; Nuzzo, R. G.; Rogers, J. A. Spin on dopants for high-performance single-crystal silicon transistors on flexible plastic substrates. *Appl. Phys. Lett.* **2005**, *86*, 133507.
(27) Fogel, D. Encapsulant characterization and doped passivated contacts for use in a luminescent solar concentrator. Colorado School of Mines, 2017. https://www.proquest.com/dissertations-theses/encapsulant-characterization-doped-passivated/docview/1925255459/se-2 (accessed November 2022).
(28) Yang, X.; Kang, J.; Liu, W.; Zhang, X.; De Wolf, S. Solution-Doped Polysilicon Passivating Contacts for Silicon Solar Cells. *ACS Appl. Mater. Interfaces* **2021**, *13*, 8455−8460.
(29) Ding, Z.; Truong, T. N.; Nguyen, H. T.; Yan, D.; Zhang, X.; Yang, J.; Wang, Z.; Zheng, P.; Wan, Y.; Macdonald, D.; Stuckelberger, J. Boron Spin-On Doping for Poly-Si/SiO_x Passivating Contacts. *ACS Appl. Energy Mater.* **2021**, *4*, 4993−4999.
(30) Kiaee, Z.; Reichel, C.; Hussain, Z.; Nazarzadeh, M.; Huyeng, J. D.; Clement, F.; Hermle, M.; Keding, R. Inkjet printing of phosphorus dopant sources for doping poly-silicon in solar cells with passivating contacts. *Sol. Energy Mater. Sol. Cells* **2021**, *222*, No. 110926.
(31) Kiaee, Z.; Fellmeth, T.; Steinhauser, B.; Reichel, C.; Nazarzadeh, M.; Nölken, A.-C.; Keding, R. TOPCon Silicon Solar Cells With Selectively Doped PECVD Layers Realized by Inkjet-Printing of Phosphorus Dopant Sources. *IEEE J. Photovoltaics* **2022**, *12*, 31−37.
(32) Sinton, R. A.; Cuevas, A. Contactless determination of current-voltage characteristics and minority-carrier lifetimes in semiconductors from quasi-steady-state photoconductance data. *Appl. Phys. Lett.* **1996**, *69*, 2510−2512.
(33) Cox, R. H.; Strack, H. Ohmic contacts for GaAs devices. *Solid-State Electron.* **1967**, *10*, 1213−1218.
(34) Alasfour, A.; Yu, Z. J.; Weigand, W.; Quispe, D.; Holman, Z. C. Sub-micrometer random-pyramid texturing of silicon solar wafers with excellent surface passivation and low reflectance. *Sol. Energy Mater. Sol. Cells* **2020**, *218*, No. 110761.
(35) Zhong, S.; Wang, W.; Tan, M.; Zhuang, Y.; Shen, W. Realization of quasi-omnidirectional solar cells with superior electrical performance by all-solution-processed Si nanopyramids. *Adv. Sci.* **2017**, *4*, No. 1700200.
(36) Baker-Finch, S. C.; McIntosh, K. R. Reflection distributions of textured monocrystalline silicon: implications for silicon solar cells. *Progr. Photovolt.: Res. Appl.* **2013**, *21*, 960−971.
(37) Karunakaran, S. K.; Arumugam, G. M.; Yang, W.; Ge, S.; Khan, S. N.; Lin, X.; Yang, G. Recent progress in inkjet-printed solar cells. *J. Mater. Chem. A* **2019**, *7*, 13873−13902.
(38) Stüwe, D.; Mager, D.; Biro, D.; Korvink, J. G. Inkjet technology for crystalline silicon photovoltaics. *Adv. Mater.* **2015**, *27*, 599−626.
(39) Martín, J.; Apraiz, A.; Aguerre, J. P.; Jimeno, J. C. Silicon Solar Cells Metallization by Industrial Inkjet Printer and Plating Process. In *27th European Photovoltaic Solar Energy Conference and Exhibition*, Frankfurt, Germany, 2012; pp 1667−1672.
(40) Park, H.; Bae, S.; Park, S. J.; Hyun, J. Y.; Lee, C. H.; Choi, D.; Kang, D.; Han, H.; Kang, Y.; Lee, H.-S.; Kim, D. Role of polysilicon in poly-Si/SiO_x passivating contacts for high-efficiency silicon solar cells. *RSC Adv.* **2019**, *9*, 23261−23266.
(41) Feldmann, F.; Bivour, M.; Reichel, C.; Hermle, M.; Glunz, S. W. Passivated rear contacts for high-efficiency n-type Si solar cells providing high interface passivation quality and excellent transport characteristics. *Sol. Energy Mater. Sol. Cells* **2014**, *120*, 270−274.
(42) Fell, A.; Altermatt, P. P. A Detailed Full-Cell Model of a 2018 Commercial PERC Solar Cell in Quokka3. *IEEE J. Photovoltaics* **2018**, *8*, 1443−1448.
(43) Messmer, C.; Fell, A.; Feldmann, F.; Wöhrle, N.; Schön, J.; Hermle, M. Efficiency Roadmap for Evolutionary Upgrades of PERC Solar Cells by TOPCon: Impact of Parasitic Absorption. *IEEE J. Photovoltaics* **2020**, *10*, 335−342.
(44) Mack, S.; Schube, J.; Fellmeth, T.; Feldmann, F.; Lenes, M.; Luchies, J. -M. Metallisation of boron-doped polysilicon layers by screen printed silver pastes. *Phys. Status Solidi: Rapid Res. Lett.* **2017**, *11*, No. 1700334.

(45) Grübel, B.; Cimiotti, G.; Schmiga, C.; Schellinger, S.; Steinhauser, B.; Brand, A. A.; Kamp, M.; Sieber, M.; Brunner, D.; Fox, S.; Kluska, S. Progress of plated metallization for industrial bifacial TOPCon silicon solar cells. *Progr. Photovolt.: Res. Appl.* **2022**, *30*, 615−621.
(46) Young, D. L.; Nemeth, W.; Grover, S.; Norman, A.; Lee, B. G.; Stradins, P. Carrier-selective, passivated contacts for high efficiency silicon solar cells based on transparent conducting oxides. In *2014 IEEE 40th Photovoltaic Specialist Conference (PVSC)*, 8−13 June 2014; pp 1−5.
(47) Hollemann, C.; Haase, F.; Schäfer, S.; Krügener, J.; Brendel, R.; Peibst, R. 26.1%-efficient POLO-IBC cells: Quantification of electrical and optical loss mechanisms. *Progr. Photovolt.: Res. Appl.* **2019**, *27*, 950−958.

Recommended by ACS

Polarization-Type Potential-Induced Degradation in Front-Emitter p-Type and n-Type Crystalline Silicon Solar Cells
Seira Yamaguchi, Atsushi Masuda, *et al.*
OCTOBER 07, 2022
ACS OMEGA
READ

Silicon–Hydrogen Bonding Configuration Modified by Layer Stacking Sequence in Silicon Heterojunction Solar Cells
Jeong-Ho An, Ka-Hyun Kim, *et al.*
DECEMBER 15, 2022
ACS APPLIED ENERGY MATERIALS
READ

Room-Temperature Fabrication of p-Type SnO Semiconductors Using Ion-Beam-Assisted Deposition
Mochamad Januar, Kou-Chen Liu, *et al.*
OCTOBER 06, 2022
ACS APPLIED MATERIALS & INTERFACES
READ

Full-Area Passivating Hole Contact in Silicon Solar Cells Enabled by a TiO_x/Metal Bilayer
Takuya Matsui, Hitoshi Sai, *et al.*
SEPTEMBER 16, 2022
ACS APPLIED ENERGY MATERIALS
READ

Get More Suggestions >

https://doi.org/10.1021/acsanm.2c04148
ACS Appl. Nano Mater. 2023, 6, 140−147